3D MODELING OF SMALL OBJECTS USING MACRO LENS IN DIGITAL VERY CLOSE RANGE PHOTOGRAMMETRY

H. Yanagi [a], H. Chikatsu [b]

[a] Architecture, Civil and Building Environmental Engineering, Graduate School of Advanced Science and Technology, Tokyo Denki University, Hatoyama, Hiki-gun, Saitama 350-0394, JAPAN - 07uda02@ms.dendai.ac.jp
[b] Department of Civil and Environmental Engineering, Tokyo Denki University, Hatoyama, Hiki-gun, Saitama 350-0394, JAPAN - chikatsu@g.dendai.ac.jp

Commission V, WG V/1

KEY WORDS: Macro lens, Zoom lens, Digital very close range photogrammetry, 3D modeling, TIN, Small object

ABSTRACT:

Recently, the documentation and visualization of various cultural assets have been receiving attention. For example, a small Buddha less than 10 cm in height and located in the womb of a larger Buddha is considered as a cultural asset. In this study, the authors have considered the use of macro lens to perform digital very close range photogrammetry for small objects. It was demonstrated that a macro lens is suitable for the documentation of small objects.
In order to evaluate 3D modeling in digital very close range photogrammetry, triplet images of a dime (diameter: 17.2 mm) were taken using a macro lens. This paper presents the ability of a macro lens for 3D modelling in digital very close range photogrammetry.

1. INTRODUCTION

Recently, digital documentation of cultural assets has been receiving attention. Small objects such as an extremely small Buddha that was located in the womb of a 12 cm tall Buddha are categorized as cultural assets. In order to document small cultural assets, convenient 3D measurements are required. Therefore, we have concentrated on the development of convenient 3D measurement software called "3DiVision" by using consumer grade digital cameras (Chikatsu *et al.*, 2006).
A stereomicroscope has been used in dental research (Mitchell *et al.*, 1989), and an enlarged image was captured using a non-metric camera with an extension tube (Hintz *et al.*, 1987). However, a zoom lens or a macro lens has generally been used for recording cultural assets or for industrial measurement.
In general, zoom lenses are used for capturing enlarged images. However, there are still problems related to the use of a zoom lens in the digital documentation of small objects. These problems include the instability of camera calibration that occurs as a result of the changes in the focal length and sharp imaging, which is caused by the depth of field. On the other hand, macro lenses have the ability to capture a sharp image of a small object from the viewpoint of the working distance.
In order to evaluate the effectiveness of macro lenses in digital very close range photogrammetry, a macro lens and a zoom lens were mounted on a digital single lens reflex camera. A comparative evaluation of the zoom lens and the macro lens has been discussed at the beginning of this paper.

In general, halation is an important issue in 3D modeling. Therefore, 3D modeling using a macro lens is discussed in the latter part of this paper with respect to halation.

2. EXPERIMENT

Table 1 lists the specifications of the zoom lens and the macro lens that were used in this investigation. These lenses were mounted on Canon EOS 20D.

Camera	Canon EOS 20D 8.2 megapixels; CMOS Sensor size: 22.5 × 15 mm
Zoom Lens	EF24-105 mm F4L IS USM Focal length: 24~105 mm F: 4
Macro Lens	EF100mm F2.8 MACRO USM Focal length: 100 mm F: 2.8

Table 1. Specifications of camera and lenses

The white square in Figure 1 shows the area that was considered in this study. The black circular targets were manufactured with an accuracy of ±0.05 mm. The diameter of each circular target was 2 cm, and the targets were arranged at intervals of 40 mm. The height of the central targets (3 rows in the centre) was 50 mm. GCPs (ground control points) and check points were arranged as shown in Figure 2. The pixel coordinates for these points were obtained as the area gravity by using image processing procedures.

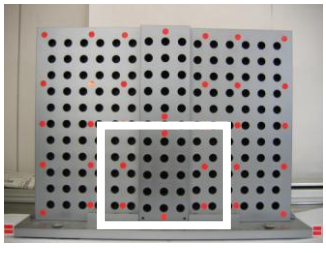

Figure 1. Test target

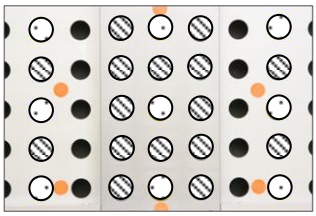

Figure 2. GCPs and check points

3. CAMERA CALIBRATION

The following 7th polynomial function with decentring distortions is a well-known lens distortion model known as the Brownian model (Brown, 1971). However, it is also well known that k_2 and k_3 in a zoom lens do not show significant influence (Wiley & Wong, 1995). Furthermore, the decentring distortion is resolved as principal point offsets (Fraser & Al-Ajlouni, 2006). Therefore, the 3rd polynomial function, which is shown in equation (2), is used in this investigation.

$$\left.\begin{aligned} x &= x' + \frac{x'}{r}(k_1 r^3 + k_2 r^5 + k_3 r^7) + p_1(r^2 + 2x'^2) + 2p_2 x'y' \\ y &= y' + \frac{y'}{r}(k_1 r^3 + k_2 r^5 + k_3 r^7) + p_2(r^2 + 2y'^2) + 2p_1 x'y' \\ r &= \sqrt{x'^2 + y'^2} \end{aligned}\right\} \quad (1)$$

where x and y are the corrected image coordinates; x' and y', image coordinates; k_1, k_2, and k_3, coefficients of radial distortion; and p_1 and p_2, coefficients of decentring distortion. r is the radial distance from the principal points.

$$\left.\begin{aligned} x &= x' + \frac{x'}{r}k_1 r^3 \\ y &= y' + \frac{y'}{r}k_1 r^3 \end{aligned}\right\} \quad (2)$$

4. VERIFICATION OF ZOOM AND MACRO LENSES

4.1 Relationship between aperture value and accuracy

The depth of field depends on the principal distance and the aperture value of the lens. For the 3D modeling of cultural assets, in particular, it is important to adjust the depth of field for each obtained image. However, appropriate imaging modes can be used to achieve superior imaging. In this study, the following three imaging modes were considered:

+ P mode (program auto exposure):
  Aperture value and shutter speed are set automatically depending on the brightness.
+ AV mode (aperture value):
  Aperture value can be changed manually.
+ A-DEP mode (auto-depth of field):
  Aperture value is set automatically depending on the AF (auto focus) frame.

The aperture value in the AV mode must be set manually. In order to decide the appropriate aperture value, five stereo images were taken at different aperture values with a base height ratio of 0.34, altitudes of 1.3 m (zoom lens) and 1.5 m (macro lens), and a focal length of 100 mm.

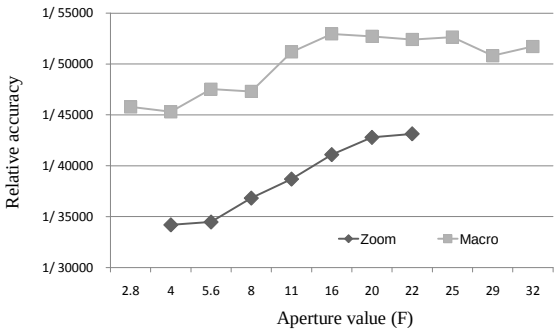

Figure 3. Relationship between aperture value and relative accuracy

$$\text{Relative accuracy} = \frac{1}{H\Big/\sqrt{\sigma_X^2 + \sigma_Y^2 + \sigma_Z^2}} \quad (3)$$

where H is the altitude; σ_X, σ_Y, and σ_Z are the root mean square errors.

Figure 3 shows the relationship between aperture values and relative accuracies. It can be seen that the relative accuracy improved with an increase in the aperture value and that the relative accuracy exhibited the highest accuracy at 22F for both lenses. However, accuracy degradation was observed over 25F in the case of the macro lens. Therefore, in this study, the aperture value in the AV mode was set at 22F.

Table 2 shows the experimental results. In terms of the accuracy for each mode, the AV mode exhibited the highest accuracy for both lenses. However, the accuracies for the A-DEP mode were similar to those of the AV mode. Therefore, it can be said that the A-DEP mode, which does not involve an adjustment of the depth of field, is a suitable imaging mode.

Zoom lens

Imaging mode	Iteration number: Left Image	Iteration number: Right Image	σ_X(mm)	σ_Y(mm)	σ_Z(mm)	Relative accuracy
P	96	127	0.0176	0.0155	0.0257	1/37970
A-DEP	58	65	0.0178	0.0143	0.0201	1/43493
AV	57	65	0.0175	0.0161	0.0187	1/43719
Standard error			0.0085	0.0085	0.0353	1/35448

Macro lens

Imaging mode	Iteration number: Left Image	Iteration number: Right Image	σ_X(mm)	σ_Y(mm)	σ_Z(mm)	Relative accuracy
P	7	7	0.0144	0.0145	0.0279	1/43463
A-DEP	7	7	0.0164	0.0125	0.0207	1/51497
AV	7	6	0.0159	0.0137	0.0192	1/52795
Standard error			0.0096	0.0096	0.0401	1/35448

Table 2. Experimental results

$$\sigma_{X0} = \sigma_{Y0} = \frac{H}{f}\sigma_p \qquad \sigma_{Z0} = \sqrt{2}\frac{H}{f}\frac{H}{B}\sigma_p \quad (4)$$

where σ_{X0}, σ_{Y0}, and σ_{Z0} are the standard errors; H is the altitude; f is the focal length; B is the baseline; and σ_P is the pointing

4.2 Enlarged imaging

In order to obtain enlarged images of small objects, it is necessary to physically approach an object. Therefore, in order to evaluate the relationship between enlarged imaging and the stability of the zoom lens and the macro lens, five triplet images were captured at five different focal lengths (60 mm, 70 mm, 80 mm, 90 mm, and 100 mm) at an altitude of 1.3 m for the zoom lens. In case of the macro lens, five triplet images were captured at different exposure

stations (2254 mm, 2025 mm, 1782 mm, 1629 mm, and 1501 mm) because the macro lens had a fixed focal length.
It should be noted that images that were taken under different focal length or different exposure station conditions appeared to be of the same size on the monitor.

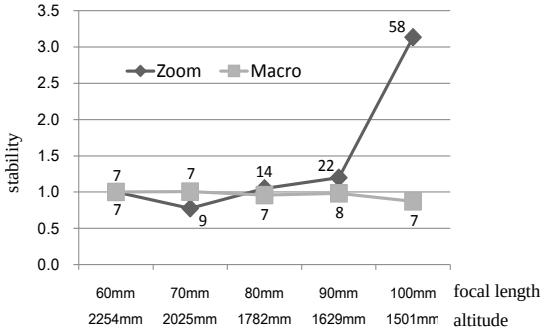

Figure 4. Stability

$$NA = \frac{\sqrt{\sigma_{Xi}^2 + \sigma_{Yi}^2 + \sigma_{Zi}^2}}{\sqrt{\sigma_{X60}^2 + \sigma_{Y60}^2 + \sigma_{Z60}^2}} \cdot \frac{R_i}{R_{60}} \qquad (5)$$

where *NA* (Normalized Accuracy) is the stability; σ_{Xi}, σ_{Yi}, and σ_{Zi} are the root mean square errors for each focal length and at each altitude; σ_{X60}, σ_{Y60}, and σ_{Z60} are the root mean square errors for the focal length of 60 mm and the altitude of 2254 mm in the case of the macro lens; R_i is the average of the iteration number for each focal length and each altitude; and R_{60} is the average of the iteration number for the focal length of 60 mm and the altitude of 2254 mm in the case of the macro lens.

The stability of the changes in the focal length setting (zoom lens) and of the changes in the exposure altitude setting (macro lens) was evaluated using equation (5). Figure 4 shows the stability. Furthermore, the numbers in Figure 4 represent the iteration numbers of the camera calibration for both the lenses.
As a result, it was deduced that the macro lens was more stable than the zoom lens because the iteration number for the macro lens was almost constant irrespective of the different altitudes. However, the iteration number for the zoom lens had extremely unstable values.

4.3 Geometric stability

In order to confirm the stability that was mentioned above with respect to the orientation parameters, five centre images for the different focal lengths (zoom lens) and different altitudes (macro lens) were investigated.
Figures 5, 6, 7, and 8 show the result of the experiment. Figures 5 and 6 show the changing ratios of the calibration parameters in the camera calibration with a focal length of 100 mm. The ratio was computed by dividing the values of the calibration parameters in each iteration by the values of the final calibration parameters. Therefore, a ratio larger than 1 implied a significant change in the camera calibration.
Figures 7 and 8 show the distance from the centre of an image to the principal point that was obtained for each iterative computation for different focal lengths (zoom lens) and different altitudes (macro lens).
From this experiment, it was observed that in the case of the zoom lens, the shifting value of the attitude angle (ω, φ) and the principal point (x_0, y_0) were large and that the amplitude attenuated exponentially, as shown in Figure 7. Additionally, it was observed that the iteration number for the camera

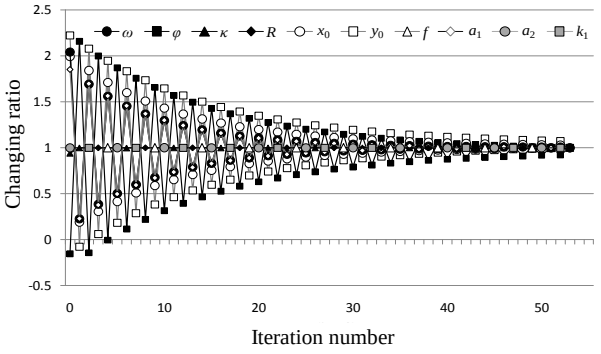

Figure 5. Ratios of calibration parameters in iteration (zoom lens)

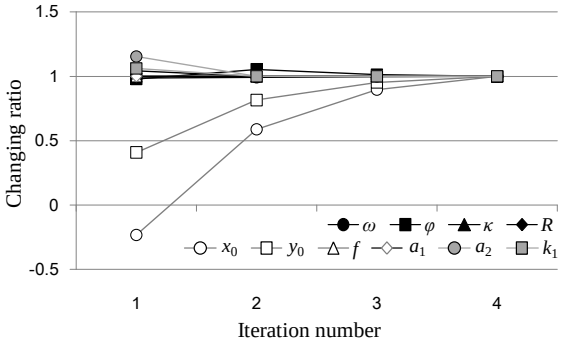

Figure 6. Ratios of calibration parameters in iteration (macro lens)

where ω, φ, and κ are the attitude angles; R is the changing ratio of the camera position for the original point; x_0 and y_0 represent the principal point; f is the focal length; a_1 and a_2 are the scale and shear factors; and k_1 is the coefficient of radial distortion.

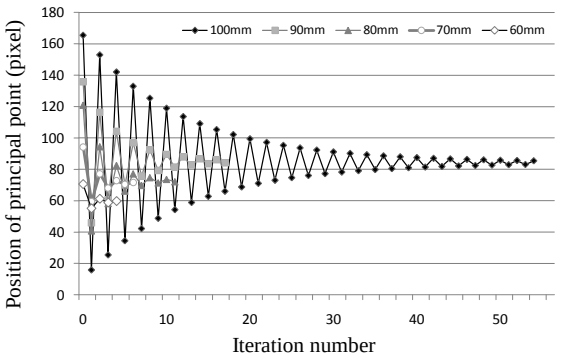

Figure 7. Relationship between changing principal point and focal length (zoom lens)

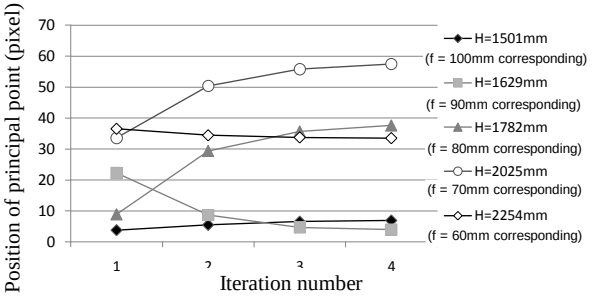

Figure 8. Relationship between changing principal point and focal length (macro lens)

calibration of the zoom lens and the position of the principal point were significant depending on the long focal length in Figures 5 and 7. On the other hand, in the case of the macro lens, the shifting value of each parameter was small, and it was observed that the iteration number of each altitude for the camera calibration of the macro lens was small for each of the parameters shown in Figures 6 and 8.
Therefore, it was inferred that the macro lens was stable.

4.4 Working distance

Working distance is defined as the length from the top of the lens to the object. In order to capture an image of a small object, it is necessary to physically approach the object. However, when the working distance is small, the image is influenced by the shadow and by the depth of field. The macro lens is capable of capturing a larger image than the zoom lens, thereby making it is unnecessary to approach the object. This was confirmed through an experiment.

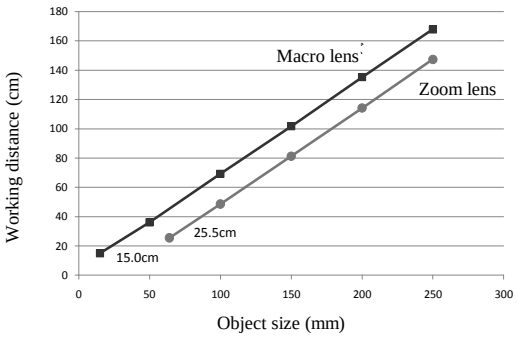

Figure 9. Working distance for capturing an image of an object

Figure 9 shows the relationship between the working distance and the size of an object. In the case of the macro lens, the image of an object of size 15 mm was captured at the working distance of 15 cm. However, the zoom lens was only capable of capturing an image of an object of size 65 mm at a working distance of 25.5 cm. Therefore, it can be inferred that the macro lens is capable of taking larger images than the zoom lens.

5. 3D MODELING

From these results, it can be concluded that macro lenses are efficient at capturing images of small objects. Therefore, in order to investigate the adaptability of the macro lens for the 3D modeling of a small object, triplet images of a dime (Figure 10) were taken by Canon EOS 20D with a macro lens and at an altitude of 365 mm. In addition, 3DiVision was used for the 3D measurement of the coin.

5.1 Image processing

In this study, the feature points for the 3D modeling of the coin were obtained by stereo matching using the left and the right images of the triplet images. However, it is difficult to obtain the feature points of the coin because the surface of the coin is approximately flat. Therefore, the feature points were increased by image processing using a Wallis filter (Jazayeri & Fraser, 2008) and a Canny filter (Canny, 1986). The Wallis filter has the characteristics of enhancing the contrast of an image, and the Canny filter has the characteristics of extracting the edges from an image.

Figures 11 and 12 show the image of Figure 10 processed by using a Wallis filter and a Canny filter, respectively.

Figure 10. A dime

Figure 11. Image processed by using a Wallis filter

Figure 12. Image processed by using a Canny filter

5.2 TIN

Generally, TIN (Triangulated Irregular Network) is used for 3D modeling. The construction of TIN models has been investigating for improving efficiency in various fields. In the field of computer geometry, for example, the flip algorithm that changes a diagonal line in a convex rectangle (Fortune, 1995), the increment algorithm that adds the point and reconstruct triangulations (Fortune, 1995), and the sweep line algorithm that constructs triangulations while scanning a plane vertically from the bottom to the top (Fortune, 1987) have been investigated. In structural mechanics, the construction of constrained TIN models that do not have triangulations in cavity areas has been investigated (Okuda, 1985).

On the other hand, halation is an important issue with respect to the capturing of an image of a cultural asset and industrial measurement, and the feature points are not obtained in a part of the halation. Therefore, the shapes around the parts of the halation in the 3D model are constructed vaguely.

Therefore, in this study, a constrained TIN model that does not have triangulations in a part of the halation was constructed by referring to the method proposed by Okuda and following the steps given below:

Step 1. Extraction of halation areas
Parts of the halation extracted by image processing and the outlines of the extracted parts are obtained.

Step 2. Construction of inclusion line
An inclusion line is constructed by using the feature points that were obtained by stereo matching and the outlines that were obtained in Step 1.

Step 3. Construction of triangulations (1)
Triangulations are constructed from a side of the inclusion line, and at the same time, triangulations are constructed from a side of the outlines that were obtained in Step 1 (Figure 13).

Step 4. Construction of triangulations (2)
Triangulations are constructed from a side of the triangulations that were constructed in Step 3. The constrained TIN model is constructed by the repetition of Step 4 (Figure 14).

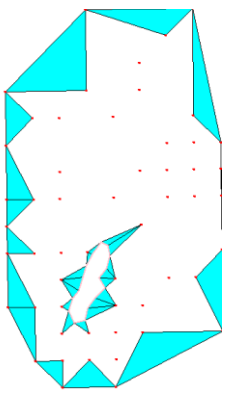

Figure 13. Construction of triangulations from one of the sides

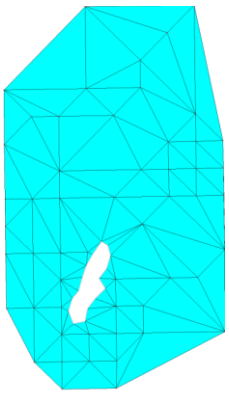

Figure 14. Constrained TIN model

Figure 15 shows the constrained TIN model of a dime; this model was constructed by following the above steps. Figure 16 shows the 3D model with texture, and Figure 17 shows a contour image of the 3D model with intervals of 0.05 mm. From these figure, it can be concluded that the 3D modeling of the dime was carried out without using parts of the halation.

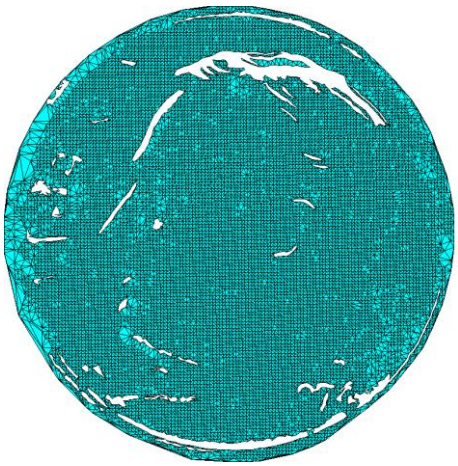

Figure 15. Constrained TIN model for the one dime coin

Figure 16. 3D model of the one dime coin with texture

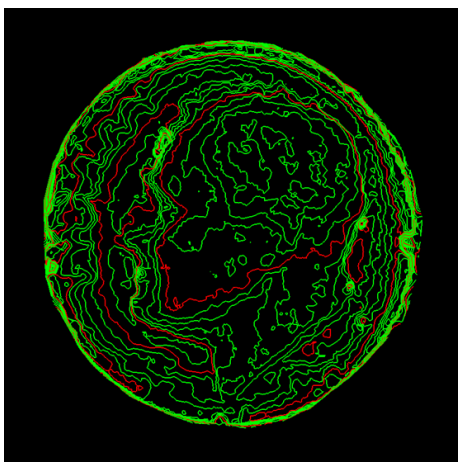

Figure 17. Contour lines

6. VERIFICATION OF 3D MODELING

In order to verify the accuracy of 3D modelling, the lengths of the dime and the 3D model were measured.
Figure 18 shows a part of the measurements of the coin and the 3D model.

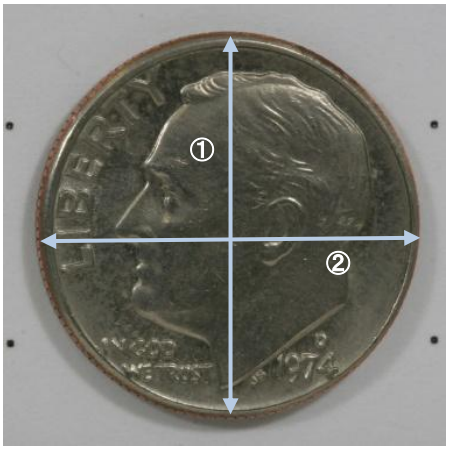

Figure 18. Part of the measurements

Measuring part	3D model	A dime
①	17.234 mm	17.2 mm
②	17.004 mm	

Table 3. Results of the measurements

From the results of the measurements of the dime, it can be concluded that the accuracy for the 3D model is almost the same value of a dime.

7. CONCLUSION

From the results presented in this paper, it can be concluded that a macro lens is efficient for small object imaging in digital very close range photogrammetry. Further, the 3D modeling of an extremely small object was achieved using a macro lens.
With respect to the capturing of images with light, halation is an important issue. However, a 3D model was constructed by using a constrained TIN model that does not construct vague shapes around parts of the halation.

References:

Chikatsu, H., Ohdake, T., 2006. Ubiquitous digital photogrammetry by consumer grade digital camera, The International Archives of the Photogrammetry, Remote Sensing and Spatial Information Sciences, Vol. XXXVI, Part 5, ISSN 1682-1750 (CD-ROM).

Mitchell, H. L., Chadwick, R. G., McCabe, J. F., 1989. Stereomicroscope photogrammetry for the measurement of small objects, Photogrammetric Record, Vol. 13, No. 74, pp. 289-299.

Hintz, R. J., Soderholm, K. J., Sarrett, D. C., 1987. Tooth morphology quantification using non-metric photography in an Analytical System, Technical Papers of the ASPRS-ACSM Annual Convention, 7, pp. 71-78.

Brown, D. C., 1971. Close-range camera calibration, Photogrammetric Engineering, Vol. 37, No. 8, pp. 855-866.

Wiley, A. G., Wong, K. W., 1995. Geometric calibration of zoom lenses for computer vision metrology, photogrammetric Engineering & Remote Sensing, Vol. 61, No. 1, pp. 69-74.

Fraser, C. S., Al-Ajlouni, S., 2006. Zoom-dependent camera calibration in digital close-range photogrammetry, Photogrammetric Engineering & Remote Sensing, Vol. 72, No. 9, pp. 1017-1026.

Schaefer, H., Murai, S., 1988. Automated target detection for real-time camera calibration, Proceeding of 9th Asian Conference on Remote Sensing, pp. H.2-4–1-H.2-4-8.

Jazayeri, I., Fraser, C. S., 2008. Interest operators in close-Range object reconstruction, The International Archives of the Photogrammetry, Remote Sensing and Spatial Information Sciences, Vol. XXXVII, Part B5, pp. 69-74.

Canny, J., 1986. A computational approach to edge detection, IEEE Transaction on Pattern Analysis and Machine Intelligence, Vol. PAMI-8, No. 6, pp. 679-698.

Fortune, S., 1995. Voronoi diagrams and delaunay triangulations, computing in euclidean geometry, World Scientific, pp. 225-265.

Fortune, S., 1987. A sweepline algorithm for voronoi diagrams, Algorithmica, 2, pp. 153-174.

Okuda, O., 1985. Automatic triangular mesh generation of arbitrary planar domains utilizing the node-pattern for finite element analysis, Journal of the Japan Society of Precision Engineering, 51(4), pp. 802-808.